Lawrence Berkeley National Laboratory

Lawrence Berkeley National Laboratory

Title
Resonant amplification of vortex-core oscillations by coherent magnetic-field pulses

Permalink
https://escholarship.org/uc/item/73j8t3nf

Author
Yu, Young-Sang

Publication Date
2013-02-01

DOI
10.1038/srep01301

Peer reviewed

eScholarship.org Powered by the California Digital Library
University of California

Resonant amplification of vortex-core oscillations by coherent magnetic-field pulses

Young-Sang Yu[1], Dong-Soo Han[1], Myoung-Woo Yoo[1], Ki-Suk Lee[1], Youn-Seok Choi[1], Hyunsung Jung[1], Jehyun Lee[1], Mi-Young Im[2], Peter Fischer[2] & Sang-Koog Kim[1]

[1]National Creative Research Initiative Center for Spin Dynamics and Spin-Wave Devices, Nanospinics Laboratory, Research Institute of Advanced Materials, Department of Materials Science and Engineering, Seoul National University, Seoul 151 -744, South Korea, [2]Center for X-ray Optics, Lawrence Berkeley National Laboratory, Berkeley CA 94720, USA.

Vortex structures in soft magnetic nanodisks are highly attractive due to their scientific beauty and potential technological applications. Here, we experimentally demonstrated the resonant amplification of vortex oscillations by application of simple coherent field pulses tuned to optimal width and time intervals. In order to investigate vortex excitations on the sub-ns time scale, we employed state-of-the-art time-resolved full-field soft X-ray microscopy of 70ps temporal and 25 nm lateral resolution. We found that, due to the resonant enhancement of the vortex gyration motion, the signal input power can be significantly reduced to , 1 Oe in field strength, while increasing signal gains, by increasing the number of the optimal field pulses. We identified the origin of this behavior as the forced resonant amplification of vortex gyration. This work represents an important milestone towards the potential implementation of vortex oscillations in future magnetic vortex devices.

Past achievements in spintronics have largely relied on an endowment of electron-charge-based electronics with novel magnetization excitation phenomena such as single-domain switching[1,2], vortex-core switching in nanomagnets[3–18], domain-wall motions in nanowires[19–23], and spin-wave excitations in magnonic crystals[24,25]. Ultrafast (~ps) magnetization excitations and their collective modes in nanomagnets have attracted interest owing to their suitability as information carriers with the additional benefit of much reduced energy dissipation compared to other electronics-based circuit devices.

A prototypic example is the study of the fundamental dynamics of vortex gyrations in single nano-size disks and their coupling in one- or two-dimensional arrays of vortex-state disks[26–29]. Since the gyration mode, representing the orbiting motions of an individual vortex core around its equilibrium position at characteristic frequencies from several hundred MHz up to ~1 GHz[30–34], is well understood and lends itself to accurate analytical predictions[35], the vortex gyration has attracted much attention it can be used as carrier for information[26–29] or as a source for microwave emission[36,37]. For implementation in future potential devices, however, the gyration amplitude must be large enough for sufficient signal gains and signal transfer fidelity in integrated functional blocks along with significant reductions in the operating power consumption[26,27,38].

Here, we experimentally investigate the resonant amplification of vortex oscillations in nanodisks by optimally tuned field pulses, by time-resolved soft X-ray microscopy measurements. The application of a series of coherent magnetic field pulses of ~~1 Oe triggers a resonant enhancement of the gyration and subsequently an increased vortex-core oscillation amplitude and, therefore, signal gain. This mechanism provides a novel and efficient way to operate reliably future devices at significantly reduced power consumption. We show that this behavior can be explained by individual force terms and their balance, as obtained from combined results of micromagnetic numerical and analytical calculations.

Results

Vortex oscillation. Figure 1a shows the spin configuration, i.e., the magnetic vortex structure, in a single circular magnetic disk. It is characterized by an out-of-plane magnetization (referred to as polarization) in the core region which can point either upward or downward, and an in-plane curling magnetization (referred to as chirality) around core which can point either counter-clockwise or clockwise[39–41]. The vortex is a stable ground state and results from the competition

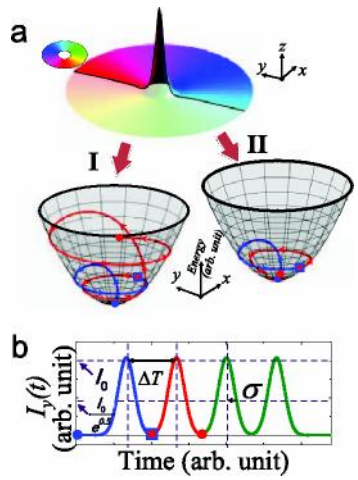

Figure 1| Concept of resonant amplification of vortex oscillations by coherent serial pulses. (a) Top: Perspective-view image and cross-section of magnetic vortex state. The color and height of the surface indicate the in- plane and out-of-plane components of local magnetizations, respectively. Bottom: Potential energy surface and analytically calcualted vortex-core trajectories. The vortex-core trajectories under the Gaussian-pulse train (pulse number N = 2) are plotted on the potential energy surface. For the cases I and II, the time intervals employed were AT= 2.0 x (27c:ND) and AT = 1.5 x (27c:ND), respectively. The blue and red lines indicate the trajectories of vortex-core positions driven by the first and second pulses, respectively (see the pulse profiles in (b)). (b) Pulses of train of Gaussian- pulse currents along single-strip electrode with pulse width (a), time interval (AT), and pulse number (N = 4).

between the short-range exchange and long-range magnetostatic interaction. For small deviations of a vortex core from its equilibrium position, the motion of a vortex the gyroforce vector of a given core polarization p, and ^D = D^I is the damping tensor with the identity matrix I^ and its damping core with its velocity v is known to be well described by Thiele's equation[42,43]: $-\mathbf{G}\times\mathbf{v}-\hat{D}\mathbf{v}+\partial W(\mathbf{X})/\partial\mathbf{X}=0$, where $\mathbf{G}=-pG\hat{\mathbf{z}}$ is the gyroforce vector of a given core polarization *p*, and $\hat{D}=D\hat{I}$ is the damping tensor with the identity matrix $\hat{I}$ and its damping constant $D < 0$ [Ref. 35]. The $W(\mathbf{X})$ is the potential energy for a displaced core position **X** and can be expressed as $W(\mathbf{X})=W(0)+\frac{1}{2}\kappa|\mathbf{X}|^2+W_{\mathrm{H}}$, where κ is the stiffness coefficient, the first term $W(0)$ the potential energy for a vortex at its initial position $\mathbf{X} = 0$, and the second term the potential energy for the shifted vortex-core position[35]. The last term, W_H, is the Zeeman energy due to a driving force if any field is externally applied. With this approach, the force-balance equation is essential to understand and predict vortex motions, which is given as $\mathbf{F}^G + \mathbf{F}^D + \mathbf{F}^W + \mathbf{F}^H = 0$, where each term corresponds to the gyroforce $\mathbf{F}^G$, the damping force $\mathbf{F}^D$, the restoring force $\mathbf{F}^W$, and the Zeeman force $\mathbf{F}^H$, respectively[35, 42, 43]. If there is no external driving force and damping, the restoring force $\mathbf{F}^W$ is in balance with the gyroforce $\mathbf{F}^G$, resulting in a persistent motion of the vortex core. If, however, there is intrinsic damping of the constituent magnetic materials (nonzero damping parameter α) a damping of core oscillations will result. In order to allow vortex-core motions to compensate or overcome such damping, external forces such as the static, alternating, or pulse form of magnetic fields or spin-polarized currents need

to be applied.

Tuning resonant amplification of vortex gyrations

Here, we focus on a mathematically simple but technologically very useful pulse form as a driving force. Figure 1b shows a serial-pulse train composed of Gaussian-shaped unipolar pulses of identical height I_0 and width σ and time interval ΔT. In the case of a damped oscillator, the motion of the vortex core can be resonantly amplified by applying a series of driving forces synchronized with the oscillatory motion of the vortex. Arbitrary driving forces would increase the oscillation amplitude whenever the driving force is in the same direction as the motion of the oscillator, but would result in a forced damping when in the opposite direction. Thus, to resonantly build up vortex-core oscillations, the driving force needs to form an in-phase repeating pattern of the same frequency as the eigenfrequency of the oscillator. Similarly, if a train of Gaussian pulses of width (σ) and time interval (ΔT) (as shown in Fig. 1b), tuned to the intrinsic resonant frequency (ω_D) of the given vortex, were applied either in-phase or out-of-phase relative to the vortex gyration, the serial successive forces would result in acceleration or damping of the vortex gyration, according to the time interval. The trajectories of the vortex core driven by two Gaussian pulses are illustrated in Fig. 1a. When the time interval is tuned to an integer of the vortex' precessional period, the amplitude of the vortex gyration can be resonantly increased, as seen in case I. By contrast, the vortex gyrations are rapidly decreased if the time interval between the first and second pulses is a half integer of the vortex precessional period, as seen in case II. On the basis of this approach, we used unipolar field pulses with an optimal width $\sigma = 1/\omega_D$ and coherent time interval $\Delta T = 2\pi/\omega_D$ (see Supplementary text online).

Soft X-ray imaging of vortex oscillations

In order to experimentally demonstrate the above described concept of resonant vortex oscillations, we fabricated a sample, as shown in Fig. 2. The sample contains several single dots, each of which consists of Permalloy (Py: $Ni_{80}Fe_{20}$) of diameter $2R$ ranging from 2.0 to 6.0 μm and a given thickness L = 40 nm (for experimental details see Methods). Trains of Gaussian current pulses applied along the y axis are simply expressed mathematically by

$$I_y = I_0 \sum_{m=0}^{N-1} \exp\left(-(t - m\Delta T - \Delta t)^2 / (2\sigma^2)\right)$$

, where N is the number of pulses in a given train. Core motions in the Py disk of diameter $2R$ = 3.0 μm were obtained by spatiotemporal-resolved full-field magnetic transmission soft X-ray microscopy (MTXM) which features a 70 ps temporal resolution and a 25 nm lateral resolution utilizing a stroboscopic pump-and-probe microscopy technique[44]. X-ray magnetic circular dichroism (XMCD) contrast near the Fe L_3 absorption edge (around 707 eV) provides magnetization orientation contrast. In our experimental setup, the in-plane curling magnetizations of the vortex were directly imaged as seen in Fig. 2b. The polarization and chirality of the Py dot were downward ($p = -1$) and counter-clockwise ($C = +1$), respectively, as determined by the rotation sense of the vortex gyration and the in-plane MTXM contrast. The optimal pulse-width (σ) value, as obtained from an experiment with single Gaussian-pulse excitation ($N = 1$), was 1.45 ns. From this value, we

could estimate a possible eigenfrequency of the real sample, here $\omega_D = 2\pi \times 110$ MHz, according to the explicit analytical form of $\sigma = 1/\omega_D$ [Refs. 17, 18].

Figure 2: Sample geometry for time-resolved soft X-ray microscopy measurement.

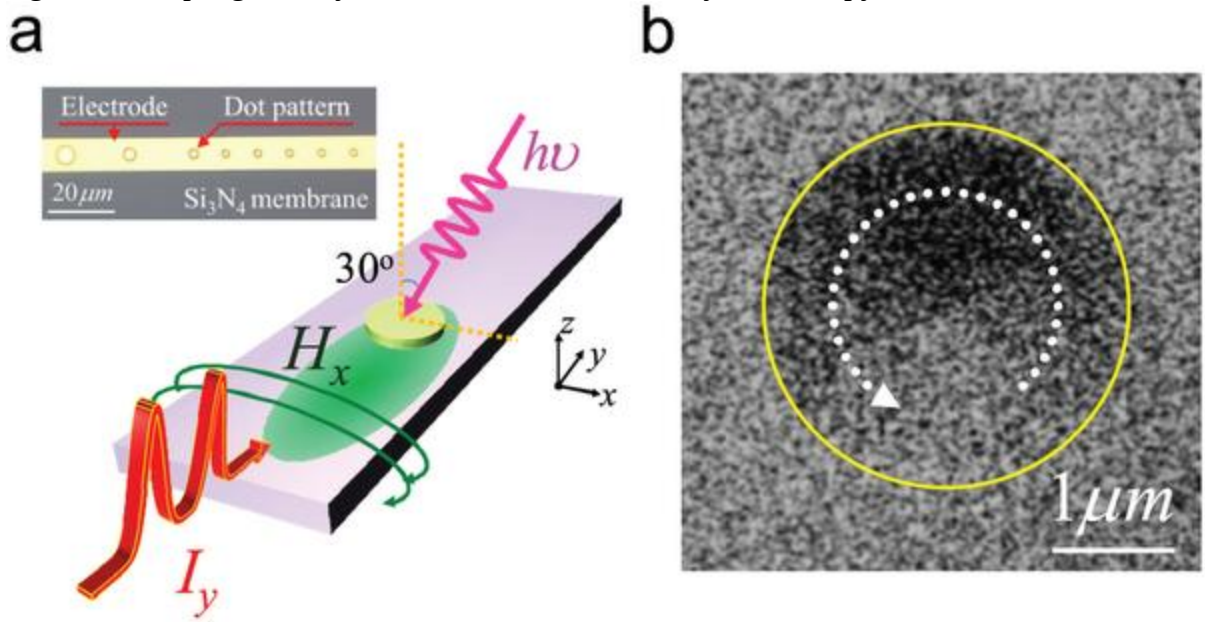

(a) Schematic drawing of sample geometry consisting of Py disks with indicated diameter $2R$ = 3.0 μm and thickness L = 40 nm and electrode of Ti (5 nm)/Cu (70 nm)/Au (5 nm). The electrode is positioned on the y-axis, thus yielding magnetic fields along the x-axis. The left-upper inset shows an optical microscopy image of the sample wherein Py disks of different diameters $2R$ = 2.0~6.0 μm are placed. The sample surface was mounted at an angle of 60° with respect to the direction of the incident X-rays. (b) MTXM image of ground vortex state of Py disk of diameter $2R$ = 3.0 μm and thickness L = 40 nm, obtained at the Fe L_3 edge. The vortex state is characterized by the CCW in-plane and downward core orientations.

As an illustration of the nontrivial motion of the vortex core in the experiment, the time-varying oscillatory x and y components of the vortex-core position and their trajectories on the disk plane as excited by two (N = 2) Gaussian pulses of field strength H_0 = 4.6 Oe are plotted in Figs. 3a and 3b, respectively, for $\Delta T = 2\pi/\omega_D$ = 9.09 ns and $\Delta T = 1.5 \times (2\pi/\omega_D)$ = 13.64 ns. Representative serial snapshot images of the XMCD contrast are shown in each second panel. In the case of $\Delta T = 2\pi/\omega_D$, where ΔT is the same as one cycle of vortex gyration, orbiting core displacement was increased with time upon application of the second pulse. By contrast, for $\Delta T = 1.5 \times (2\pi/\omega_D)$, the core gyration amplitude rapidly decreased after application of the second pulse.

Figure 3: (a) Amplification and (b) damping of vortex oscillations.

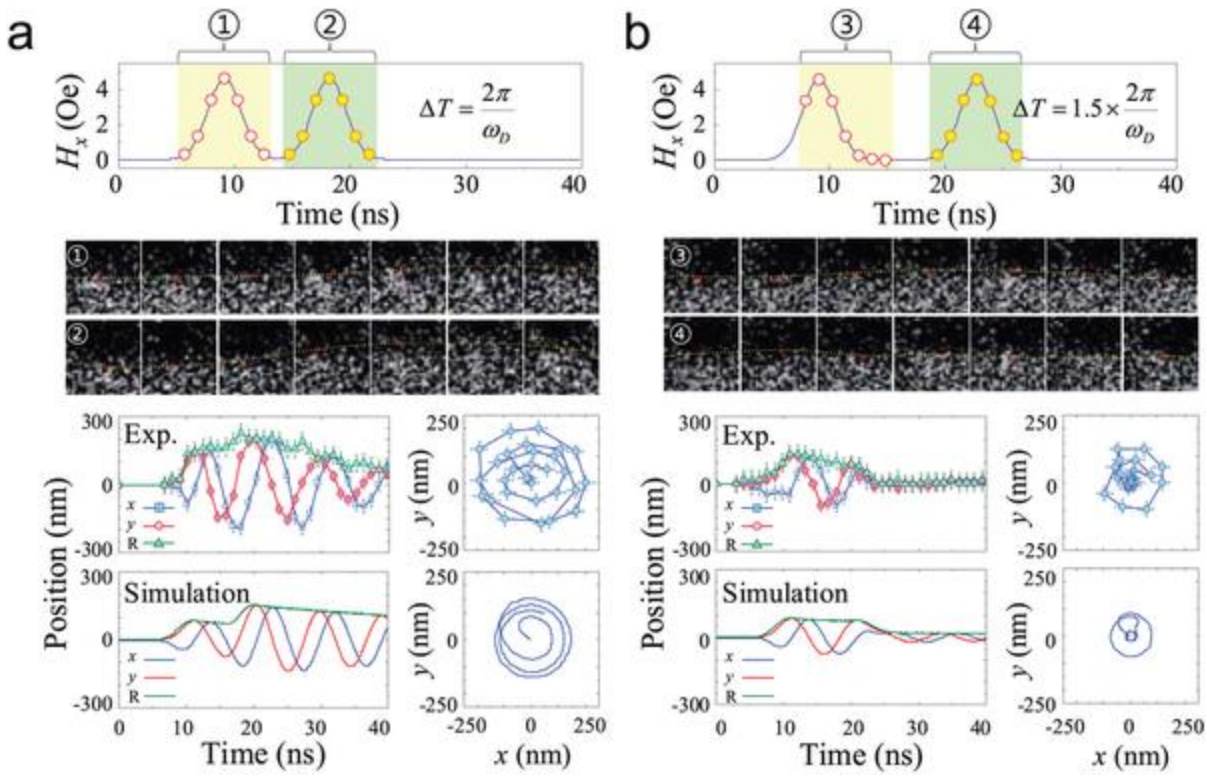

The first row shows the profiles of two serial field pulses of (a) $\Delta T = 1.0 \times (2\pi/\omega_D)$ and (b) $\Delta T = 1.5 \times (2\pi/\omega_D)$. In the second row of (a) and (b), there are serial snapshot XMCD images of the temporal evolution of vortex-core motions. The red and yellow symbols in the first row indicate the snapshot time for each image. The third row indicates the *x*- and *y*-components and displacement of the vortex-core positions (left) from the center position (*x*, *y*) = (0, 0) and the constructed vortex-core trajectories (right), as obtained from the time-resolved MTXM images; the fourth row shows the corresponding simulation results.

Analytical calculation and numerical simulation

To interpret the experimentally observed core gyration amplitude asymmetry (amplification versus damping), we conducted micromagnetic simulations (see Methods for details). The results are shown in the fourth rows of Figs. 3a and 3b, and are in excellent agreement with the experimental results, except for slight deviations in their oscillation amplitudes and frequencies. These discrepancies can be attributed to sample imperfections or several possible simulation/experiment deviations in the dimensions, material parameters and field strength. Then, based on Thiele's analytical approach[42, 43], for a given magnetization structure taken at a certain time and a given core velocity **v**, all of the forces can be calculated directly from the integrations of the magnetization configurations that were obtained from the micromagnetic numerical simulations. The individual forces are as follows: $\mathbf{F}^G = -G(\hat{\mathbf{z}} \times \mathbf{v})$ with $G = (L/\gamma M_s^2) \int_S \mathbf{M} \cdot [(\partial \mathbf{M}/\partial x_1) \times (\partial \mathbf{M}/\partial x_2)] dS$, the damping force $\mathbf{F}^D = \hat{D} \cdot \mathbf{v} = \sum \hat{D}_{ij} v_j$,

where a damping tensor $\hat{D}_{ij} = -(\alpha L/\gamma M_s)\int_S [(\partial \mathbf{M}/\partial x_i)\cdot(\partial \mathbf{M}/\partial x_j)]\,dS$ with the damping constant α, the gyromagnetic ratio γ, and the saturation magnetization M_s. The restoring force and Zeeman force are given as $F_i^W + F_i^H = -\int H_j^{\text{eff}}(\partial M_j/\partial x_i)\,dV$ with the effective field $\mathbf{H}^{\text{eff}} = \delta W/\delta \mathbf{M}$. From these relations, the Zeeman force can be descried as $\mathbf{F}^H = -\int (\delta W_{\text{H}}/\delta \mathbf{M})(\partial \mathbf{M}/\partial x_i)\,dV$, where $W_{\text{H}} = -\mu(\hat{\mathbf{z}} \times \mathbf{H})\cdot\mathbf{X}$ with $\mu = \pi R L M_s \xi C$ ($\xi = 2/3$ for the "side-charge-free" model[35]).

Accordingly, the resultant core motion can be determined from the numerically estimated individual forces, as represented by the magnitudes and directions of all of the forces. For the two cases of $1.0 \times (2\pi/\omega_D)$ and $1.5 \times (2\pi/\omega_D)$, temporal variations of the force magnitude and orientation are plotted in Figs. 4a and 4b, respectively. The definition of the force orientation (θ) is illustrated in Fig. 4c. The first Gaussian pulse excites the precessional motion of the vortex core from its initial position **X** = 0; if the second Gaussian pulse is applied, the Zeeman force $\mathbf{F}^H$ is generated, and thus, to compensate the Zeeman force $\mathbf{F}^H$, the magnitude and orientation of gyroforce $\mathbf{F}^G$ and restoring force $\mathbf{F}^W$ change. Fig. 4a and 4b show the angles and amplitudes of the Zeeman force $\mathbf{F}^H$ and restoring force $\mathbf{F}^W$ in response to the vortex-core position vector **X** and applied magnetic field **H**. When the second Gaussian pulse is applied with the time interval (ΔT) of an integer of the vortex precessional period $1.0 \times (2\pi/\omega_D)$, the Zeeman force $\mathbf{F}^H$ induced by the second pulse is in-phase relative to the vortex core orbiting around the center position. To satisfy the force balance, the angle of the gyroforce $\mathbf{F}^G$ has the negative angle, and the magnitude of gyroforce $\mathbf{F}^G$ and restoring force $\mathbf{F}^W$ increase as shown in Fig. 4a. As a result, the angle of the vortex velocity vector **v** is an acute angle due to the relation of $\mathbf{F}^G = -G(\hat{\mathbf{z}} \times \mathbf{v})$. This means that the radius of the vortex gyration is increased according to the resultant velocity vector, as shown in the first schematic image in Fig. 4d (the damping force $\mathbf{F}^D$ is not shown here for simplicity). In the same manner, the Gaussian-pulse train with the time interval of a half integer of the vortex precessional period $[\Delta T = 1.5 \times (2\pi/\omega_D)]$ can reduce the radius of the vortex gyration, as shown in the second image in Fig. 4d.

Figure 4: Force-balance relation in vortex oscillation.

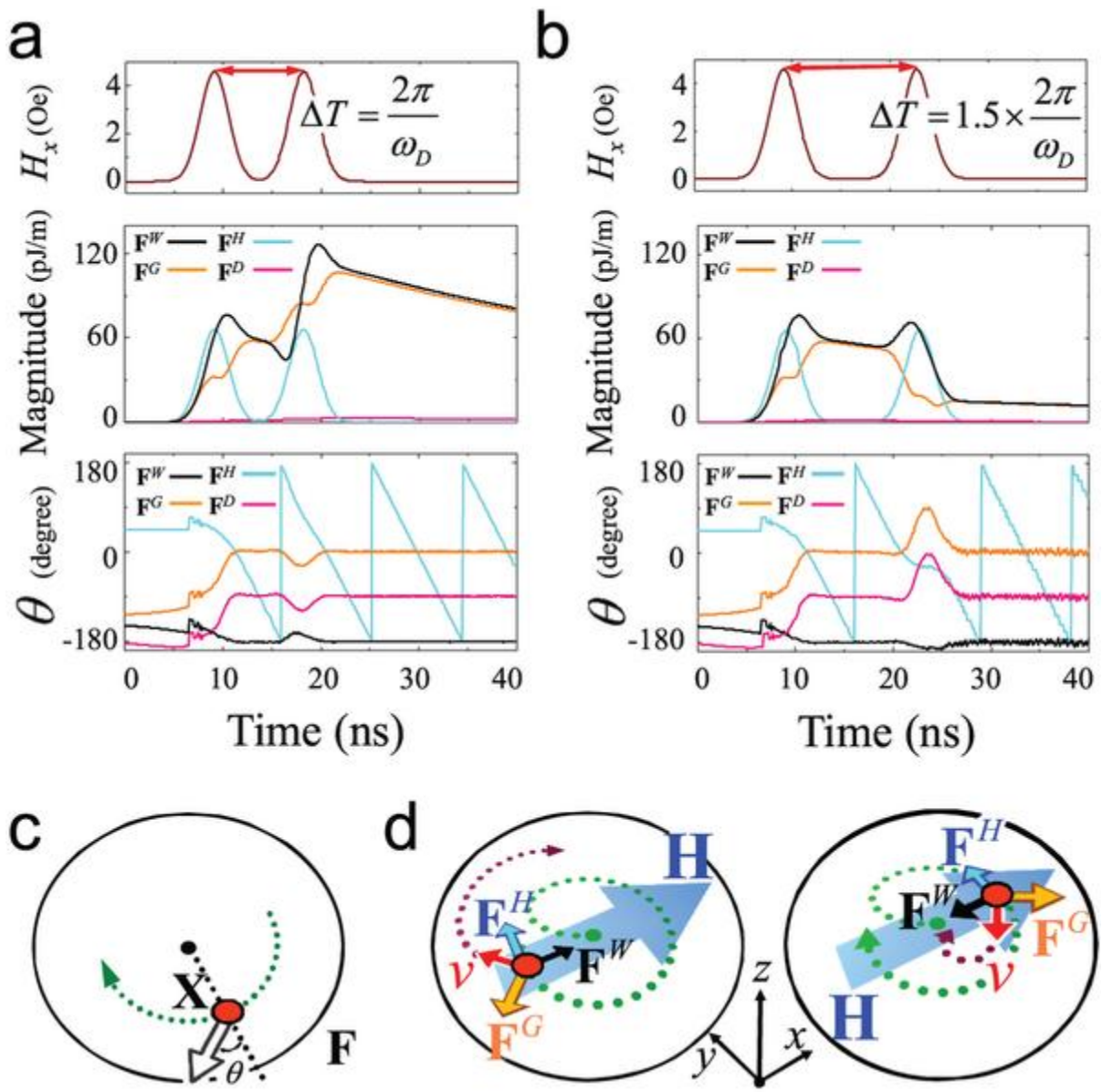

(a, b) The second row presents the strengths of the individual force terms, that is, the gyroforce $\mathbf{F}^G$, the Zeeman forces $\mathbf{F}^H$, the restoring force $\mathbf{F}^W$, and the damping forces $\mathbf{F}^D$, according to the applied Gaussian-pulse fields shown in the first row. The bottom row shows the orientations of the individual force terms, that is, the angles θ with respect to the vortex-core-position vector ($\mathbf{X}$), as defined in (c). (d) Schematic illustration of orientation and strength of employed forces under resonant amplification (left) and forced damping (right), where for simplification, damping force $\mathbf{F}^D$ is not shown. $\mathbf{v}$ corresponds to the core motion velocity vector. The red dot indicates the core position.

Furthermore, we experimentally observed the maximum core displacement $|\mathbf{X}|_{max}$ versus $\Delta T/\Delta T_0$ ($\Delta T_0 = 2\pi/\omega_D$= 9.09 ns, $0.5 \times \Delta T_0$to $2.0 \times \Delta T_0$) by applying a sequence of two Gaussian pulses of field strength H_0 = 4.6 Oe and optimal width $\sigma = 1/\omega_D$= 1.45 ns. The experimental results (closed circles) of $|\mathbf{X}|_{max}$ are compared with the analytical calculations (solid line), as

shown in Fig. 5. As predicted by the analytical form of $\Delta T = m \times (2\pi/\omega_D)$, the integer values of *m* evidenced amplification of vortex gyration, whereas the half integers showed further damping of the vortex gyration. This implies that the time at which the second pulse arrives plays a role in the in-phase and out-of-phase motions of the vortex core.

Figure 5: Maximum vortex-core displacement $|X|_{max}$ for different time intervals, $\Delta T/\Delta T_0$= 0.5~2.0, where $\Delta T_0 = 2\pi/\omega_D$, along with identical parameters of pulse number N = 2, $\sigma = 1/\omega_D$ = 1.45 ns, and H_0 = 4.6 Oe.

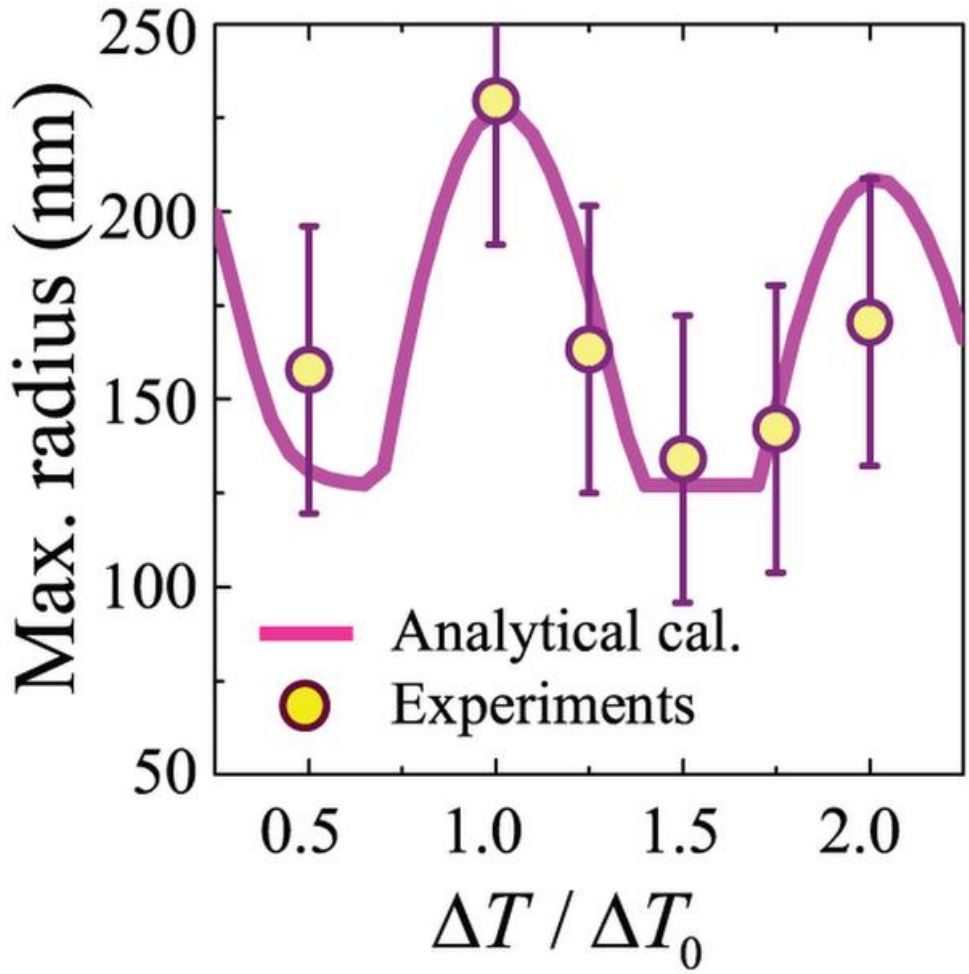

The yellow dots and solid line correspond to the experimental results and analytical calculation, respectively.

Impact of pulse number on the resonant amplification

Next, we experimentally examined the core displacement as a function of time for a different pulse number N (= 1, 2, 3, 4, 5) for the optimal width σ = 1.45 ns, time interval ΔT = 9.09 ns, and field strength H_0 = 4.6 Oe, as plotted in Fig. 6. The inset in Fig. 6 shows the corresponding simulation results for the real Py disk and explains well how the core displacement increases with the number of coherent optimized field pulses. Figure 7a shows the maximum displacement

of the core position for N = 1, 2, 3, 4, and 5, as obtained from Fig. 6, and provides evidence that the amplification of the vortex-core gyration by N = 5 is three times greater than that by N = 1. In Fig. 7b, for N = 10, the maximum displacement is plotted with H_0, indicating that with application of more Gaussian pulses, a sufficient displacement of core motion, 200 nm (1/7.5 of the disk radius), can be achieved with the extremely low field strength of 2 Oe. Interpolation of this data showed that with 1 Oe, 100 nm displacement can be achieved.

Figure 6: Vortex-core displacement as function of time according to different number of coherent pulses.

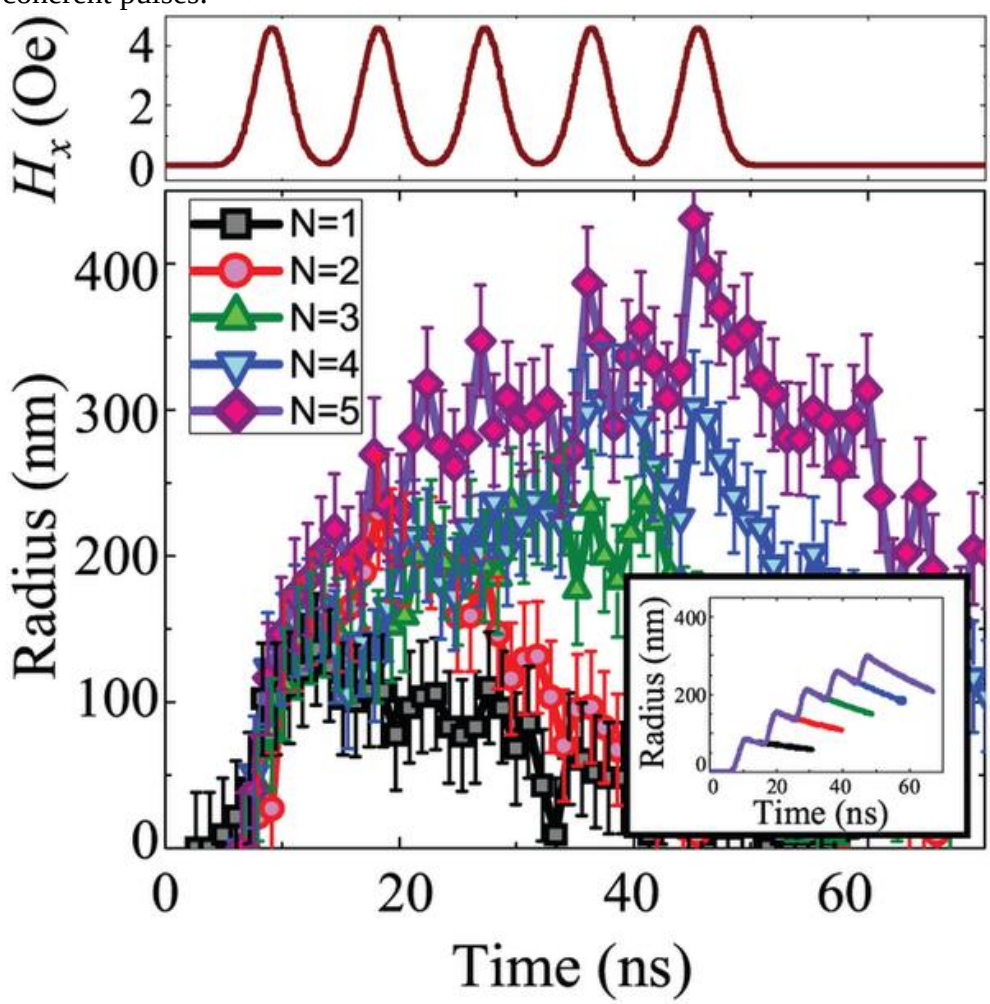

The trains of Gaussian magnetic field pulses under the optimal conditions $\sigma = 1/\omega_D = 1.45$ns, ΔT = $1.0 \times (2\pi/\omega_D) = 9.09$ns, and field strength H_0 = 4.6 Oe were applied. The pulse profile according to the time is shown in the first row. The right inset shows the corresponding simulation results obtained under the same conditions as those prevailing in the experiment.

Figure 7: Experimental results of maximum vortex-core displacement versus pulse number in (a) and versus H_0 in (b).

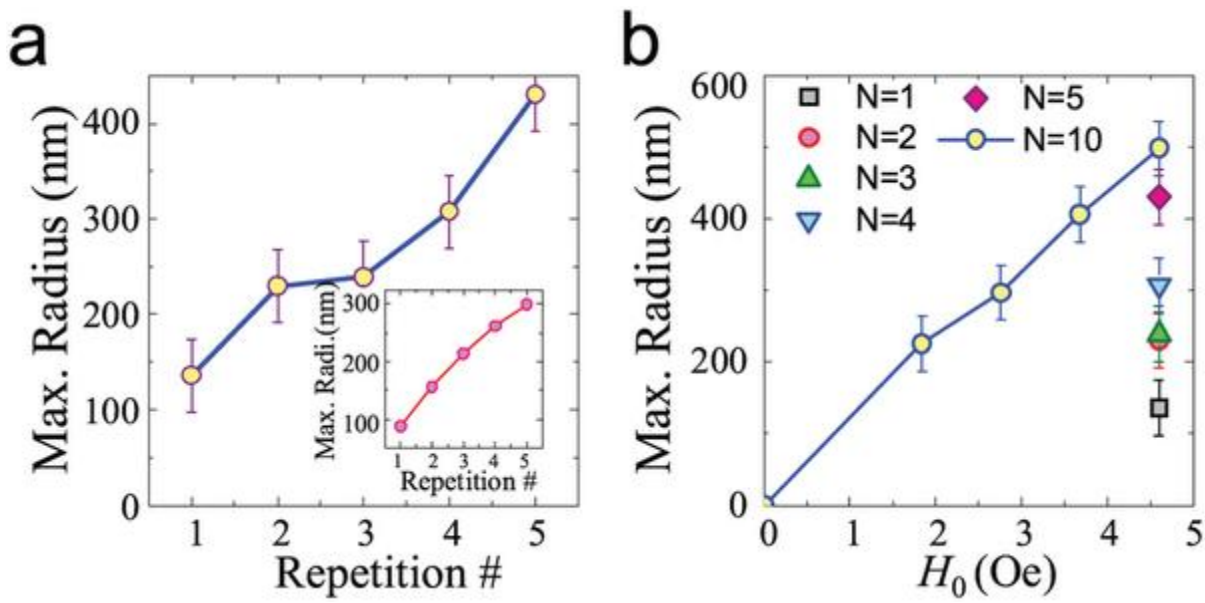

The trains of Gaussian magnetic field pulses under the optimal conditions $\sigma = 1/\omega_D = 1.45$ns, $\Delta T = 1.0 \times (2\pi/\omega_D) = 9.09$ns were applied. For comparison, the results in (a) also are plotted in (b).

Discussion

We experimentally demonstrated that the resonant excitation and amplification of vortex gyrations can be achievable with extremely low power consumption as much as ~1 Oe by application of a series of coherent Gaussian pulses of optimal interval $\Delta T = 2\pi/\omega_D$and pulse width $\sigma = 1/\omega_D$. Signal gain can be defined as the mean ratio of the final vortex-gyration amplitude to the initial vortex gyration. Therefore, a large displacement of vortex gyration indicates a sufficient signal gain detectable through Tunnel magnetoresistance[45] (TMR) or Giant magnetoresistance[46, 47] (GMR) in possible spin value structures. Since signal gain in electronic devices is a measure of the capacity to increase the power or amplitude of a signal from input to output. The present work quantitatively clarifies the fundamental of vortex excitations and their amplifications, and might provide a way to significantly amplify vortex-gyration-based signal gains in future devices at considerably reduced power consumption (~1 Oe in field strength).

Methods

Sample fabrication

For the measurement of soft X-ray transmission through the sample, all of the disks and electrodes were prepared on 100-nm-thick silicon nitride (Si_3N_4) membranes. The 40 nm-thick Py films were deposited by magnetron sputtering under base pressures of less than 5×10^{-9} Torr. Py disks of radius $2R$ = 2.0~6.0 μm were patterned by typical e-beam lithography (Jeol, JBX9300FS) and subsequent lift-off processes. Each disk was placed on a strip electrode composed of Ti (5 nm)/Cu (70 nm)/Au (5 nm) and patterned, like the Py disks, by e-beam lithography and subsequent lift-off processes.

Time-resolved soft X-ray microscopy measurement

Snapshot images of vortex-core oscillations were measured by full-field soft X-ray transmission microscopy at the Advanced Light Source (Beamline 6.1.2) in Berkeley, California, USA, using a stroboscopic pump-and-probe technique[44]. The microscopy boasts a temporal resolution of 70 ps and a lateral resolution of less than 25 nm. The in-plane magnetization contrast was provided by X-ray magnetic circular dichroism (XMCD) near the Fe L_3 absorption edge (around 707 eV), according to the in-plane geometry whereby the sample was mounted at an angle of 60° with respect to the propagation direction of incident X-rays. In order to achieve adequate XMCD contrasts, 10 to 20 individual images were accumulated. The structural contrast was normalized to an image obtained under a saturation field. Based on a stroboscopic pump-and-probe technique[44], Trains of Gaussian-shaped field pulses were synchronized to X-ray pulses of ~3 MHz frequency, and the time delay between the pulse trains and the incident X-ray was varied from 0 to 60 ns in increments of 1.14 ns (eight images per cycle of vortex gyration, at a frequency of 110 MHz). In the experiment, a Gaussian current pulse was applied with an arbitrary waveform generator. The height of the output pulse voltage was measured as 350~370 mV with an oscilloscope with an impedance of Z = 50 Ohm, which corresponds to 0.7~0.74 transmittance. On the basis of Ampere's Law, we estimated the resultant Oersted field strength and spatial distribution with the measured output voltage and the impedance of the oscilloscope employed. Accordingly, the field strength was determined to be H_0 = 4.6 Oe at the center of the Py disk (20 nm from the electrode surface). The local distribution of the magnetic field was calculated using the analytical equations shown in Ref. 48.

Micromagnetic simulations

Micromagnetic simulations were carried out for a model system of the same dimensions as those of the sample and under the same conditions as those in the experiment. To numerically simulate the vortex-core oscillations, we employed the OOMMF code[49], which utilizes the Landau-Lifshitz-Gilbert equation of motion of magnetization: $\partial \mathbf{M}/\partial t = -\gamma(\mathbf{M} \times \mathbf{H}_{\mathrm{eff}}) + \alpha/|\mathbf{M}|(\mathbf{M} \times \partial \mathbf{M}/\partial t)$) [Ref. 50 and 51], with the gyromagnetic ratio γ (2.21 × 10^5 m/As) and the phenomenological damping constant α (0.01). We used a unit cell size of 4 × 4 × 40 nm^3. To match the eigenfrequency of the model to that of the sample ($\omega_D = 2\pi \times 110$ MHzMHz), we used M_s = 7.6 × 10^5 A/m for the numerical simulations[4, 52, 53]. The other simulation parameters for Py were as follows: exchange stiffness A_{ex} = 1.3 × 10^{-11} J/m and magnetocrystalline anisotropy constant K = 0.

References

1. Cowburn, R. P. & Welland, M. E. Room temperature magnetic quantum cellular automata. Science 287, 1466–1468 (2000).
2. Imre, A. *et al.* Majority logic gate for magnetic quantum-dot cellular automata. Science 311, 205–208 (2006).
3. Van Waeyenberge, B. *et al.* Magnetic vortex core reversal by excitation with short bursts of an alternating field. Nature 444, 461–464 (2006).
4. Yamada, K. *et al.* Electrical switching of the vortex core in a magnetic disk. Nature Mater. 6, 269–273 (2007).
5. Hertel, R., Gliga, S., Fähnle, M. & Schneider, C. M. Ultrafast nanomagnetic toggle switching of vortex cores. Phys. Rev. Lett. 98, 117201 (2007).
6. Lee, K.-S., Guslienko, K. Y., Lee, J.-Y. & Kim, S.-K. Ultrafast vortex-core reversal dynamics in ferromagnetic nanodots. Phys. Rev. B 76, 174410 (2007).

7. Kim, S.-K. *et al.* Electric-current-driven vortex-core reversal in soft magnetic nanodots. Appl. Phys. Lett. 91, 082506 (2007).
8. Kravchuk, V. P., Sheka, D. D., Gaididei, Y. & Merten, F. G. Controlled vortex core switching in a magnetic nanodisk by a rotating field. J. Appl. Phys. 102, 043908 (2007).
9. Guslienko, K. Y., Lee, K.-S. & Kim, S.-K. Dynamic origin of vortex core switching in soft magnetic nanodots. Phys. Rev. Lett. 100, 027203 (2008).
10. Lee, K.-S. *et al.* Universal criterion and phase diagram for switching a magnetic vortex core in soft magnetic nanodots. Phys. Rev. Lett. 101, 267206 (2008).
11. Curcic, M. *et al.* Polarization selective magnetic vortex dynamics and core reversal in rotating magnetic fields. Phys. Rev. Lett. 101, 197204 (2008).
12. Kim, S.-K., Lee, K.-S., Choi, Y.-S. & Yu, Y.-S. Low-power selective control of ultrafast vortex-core switching by circularly rotating magnetic fields: Circular–rotational eigenmodes. IEEE Trans. Mag. 44, 3071–3074 (2008).
13. Vansteenkiste, A. *et al.* X-ray imaging of the dynamic magnetic vortex core deformation. Nature Phys. 5, 332–334 (2009).
14. Weigand, M. *et al.* Vortex core switching by coherent excitation with single in-plane magnetic field pulses. Phys. Rev. Lett. 102, 077201 (2009).
15. Kravchuk, V. P., Gaididei, Y. & Sheka, D. D. Nucleation of a vortex-antivortex pair in the presence of an immobile magnetic vortex. Phys. Rev. B 80, 100405R (2009).
16. Kammerer, M. *et al.* Magnetic vortex core reversal by excitation of spin waves. Nat. Commun. 1, 279 (2011).
17. Yu, Y.-S. *et al.* Polarization-selective vortex-core switching by tailored orthogonal Gaussian-pulse currents. Phys. Rev. B 83, 1744299 (2011).
18. Yu, Y.-S. *et al.* Memory-bit selection and recording by rotating fields in vortex-core. Appl. Phys. Lett. 98, 052507 (2011).
19. Allwood, D. A. *et al.* Submicrometer ferromagnetic NOT gate and shift register. Science 296, 2003–2006 (2002).
20. Allwood, D. A. *et al.* Magnetic domain-wall logic. Science 309, 1688 (2005).
21. Yamanouchi, M. *et al.* Current-induced domain-wall switching in a ferromagnetic semiconductor structure. Nature 428, 539–542 (2004).
22. Parkin, S. S. P., Hayashi, M. & Thomas, L. Magnetic domain-wall racetrack memory. Science 320, 190–194 (2008).
23. Hayashi, M. *et al.* Current-controlled magnetic domain-wall nanowire shift register. Science 320, 209–211 (2008).
24. Choi, S., Lee, K.-S., Guslienko, K. Y. & Kim, S.-K. Strong radiation of spin waves by core reversal of a magnetic vortex and their wave behaviours in magnetic nanowire waveguides. Phys. Rev. Lett. 98, 087205 (2007).
25. Lee, K.-S., Han, D.-S. & Kim, S.-K. Physical origin and generic control of magnonic band gaps of dipole-exchange spin waves in width-modulated-nanostrip waveguides. Phys. Rev. Lett. 102, 127202 (2009).
26. Jung, H. *et al.* Observation of coupled vortex gyrations by 70-ps-time- and 20-nm-spaceresolved full-field magnetic transmission soft x-ray microscopy. Appl. Phys. Lett. 97, 222502 (2010).
27. Jung, H. *et al.* Tunable negligible-loss energy transfer between dipolar-coupled magnetic disks by stimulated vortex gyration. Sci. Rep. 1, 59 (2011).
28. Vogel, A. *et al.* Coupled vortex oscillations in spatially separated permalloy squares. Phys. Rev. Lett. 106, 137201 (2011).
29. Sugimoto, S. *et al.* Dynamics of coupled vortices in a pair of ferromagnetic disks. Phys. Rev. Lett. 106, 197203 (2011).

30. Lee, K.-S. & Kim, S.-K. Two circular-rotational eigenmodes and their giant resonance asymmetry in vortex gyrotropic motions in soft magnetic nanodots. Phys. Rev. B 78, 014405 (2008).
31. Park, J. P. *et al.* Imaging of spin dynamics in closure domain and vortex structures. Phys. Rev. B 67, 020403 (2003).
32. Choe, S.-B. *et al.* Vortex core–driven magnetization dynamics. Science 304, 420–422 (2004).
33. Kasai1, S. *et al.* Current-driven resonant excitation of magnetic vortices. Phys. Rev. Lett. 97, 107204 (2006).
34. Bolte, M. *et al.* Time-resolved X-ray microscopy of spin-torque-induced magnetic vortex gyration. Phys. Rev. Lett. 100, 176601 (2008).
35. Guslienko, K. Y. *et al.* Eigenfrequencies of vortex state excitations in magnetic submicron-size disks. J. Appl. Phys. 91, 8037–8039 (2002).
36. Dussaux, A. *et al.* Large microwave generation from currentdriven magnetic vortex oscillators in magnetic tunnel junctions. Nat. Commun. 1, 8 (2010).
37. Pribiag, V. S. *et al.* Magnetic vortex oscillator driven by d.c. spin-polarized current. Nature Phys. 3, 498–503 (2007).
38. Barman, S., Barman, A. & Otani, Y. Controlled propagation of locally excited vortex dynamics in linear nanomagnet arrays. J. Phys. D: Appl. Phys. 43, 335001 (2010).
39. Shinjo, T. *et al.* Magnetic vortex core observation in circular dots of Permalloy. Science 289, 930–932 (2000).
40. Wachowiak, A. *et al.* Direct observation of internal spin structure of magnetic vortex cores. Science 298, 577–580 (2002).
41. Cowburn, R. P. Spintronics: Change of direction. Nature Mater. 6, 255–256 (2007).
42. Thiele, A. A. Steady-state motion of magnetic domains. Phys. Rev. Lett. 30, 230–233 (1973).
43. Huber, D. L. Dynamics of spin vortices in two-dimensional planar magnets. Phys. Rev. B 26, 3758–3765 (1982).
44. Fischer, P. *et al.* Soft X-ray microscopy of nanomagnetism. Mater. Today 9, 26 (2006).
45. Julliere, M. Tunneling between ferromagnetic films. Phys. Lett. A 54, 225 (1975).
46. Binasch, G., Grünberg, P., Saurenbach, F. & Zinn, W. Enhanced magnetoresistance in layered magnetic structures with antiferromagnetic interlayer exchange. Phys. Rev. B 39, 4828 (1989).
47. Fert, A. *et al.* Giant magnetoresistance of (001)Fe/(001)Cr magnetic superlattices. Phys. Rev. Lett. 61, 2472 (1988).
48. Chumakov, D. *et al.* Nanosecond time-scale switching of permalloy thin film elements studied by wide-field time-resolved Kerr microscopy. Phys. Rev. B 71, 014410 (2005).
49. See http://math.nist.gov/oommf. (May2007).
50. Landau, L. D. & Lifshitz, E. M. On the theory of the dispersion of magnetic permieability in ferromagnetic bodies. Phys. Z. Sowjetunion 8, 153 (1935).
51. Gilbert, T. L. A phenomenological theory of damping in ferromagnetic materials. IEEE Trans. Mag. 4, 3443 (2004).
52. Novosad, V. *et al.* Magnetic vortex resonance in patterned ferromagnetic dots. Phys. Rev. B 72, 024455 (2005).
53. Guslienko Yu, K. *et al.* Magnetic Vortex Core Dynamics in Cylindrical Ferromagnetic Dots. Phys. Rev. Lett. 96, 067205 (2006).

Acknowledgements

This research was supported by the Basic Science Research Program administered under the auspices of the National Research Foundation of Korea (NRF), which is funded by the Ministry of Education, Science, and Technology (Grant No. 20120000236). The operation of the soft X-ray microscope was supported by the Director, Office of Science, Office of Basic Energy Sciences, Materials Sciences and Engineering Division, U.S. Department of Energy under Contract No. DE-AC02-05-CH11231.

DISCLAIMER

This document was prepared as an account of work sponsored by the United States Government. While this document is believed to contain correct information, neither the United States Government nor any agency thereof, nor The Regents of the University of California, nor any of their employees, makes any warranty, express or implied, or assumes any legal responsibility for the accuracy, completeness, or usefulness of any information, apparatus, product, or process disclosed, or represents that its use would not infringe privately owned rights. Reference herein to any specific commercial product, process, or service by its trade name, trademark, manufacturer, or otherwise, does not necessarily constitute or imply its endorsement, recommendation, or favoring by the United States Government or any agency thereof, or The Regents of the University of California. The views and opinions of authors expressed herein do not necessarily state or reflect those of the United States Government or any agency thereof or The Regents of the University of California.